AIP | Journal of Applied Physics

Prediction of blind frequency in lock-in thermography using electro-thermal model based numerical simulation

Krishnendu Chatterjee and Suneet Tuli

Citation: Journal of Applied Physics **114**, 174905 (2013); doi: 10.1063/1.4828480
View online: http://dx.doi.org/10.1063/1.4828480
View Table of Contents: http://scitation.aip.org/content/aip/journal/jap/114/17?ver=pdfcov
Published by the AIP Publishing

JOURNAL OF APPLIED PHYSICS **114**, 174905 (2013)

Prediction of blind frequency in lock-in thermography using electro-thermal model based numerical simulation

Krishnendu Chatterjee and Suneet Tuli
Centre for Applied Research in Electronics, Indian Institute of Technology, Delhi, India

(Received 3 August 2013; accepted 16 October 2013; published online 4 November 2013)

Lock-in thermography is increasingly becoming popular as a non-destructive testing technique for defect detection in composite materials for its low heating excitation. The experimental data is processed with Fourier transformation to produce phase and amplitude images. Phase images, though immune to surface emissivity variation, suffer from blind frequency effect, where a defect becomes invisible at a certain excitation frequency. There exists no analytical model to predict this 3-dimensional heat flow phenomenon. This paper presents a study of blind frequency using electro-thermal model based numerical simulation on a piece of thermally anisotropic carbon fibre composite. The performance of the simulator is optimized for spatial mesh size. Further the effect of paint layer, which is often applied to the sample surface for better thermal imaging, has been incorporated in the simulation. Finally, both experimental and simulation results are presented side-by-side for easy comparison. *© 2013 AIP Publishing LLC*.
[http://dx.doi.org/10.1063/1.4828480]

I. INTRODUCTION

Thermal non-destructive testing (TNDT) has become popular in recent years. It uses the surface temperature profile of the test piece to predict its health. Infra-red thermal imaging (IR-thermography) is extensively used for this purpose. TNDT is divided into two categories—passive and active. The former relies on self-heating of the test piece, while the latter deploys heating by external stimuli. Passive tests are primarily used for preventive maintenance, e.g., day time fire detection, in-circuit component health monitoring, vehicle break system and lubrication inspection. Active tests are used for sub-surface defect detection. Without the external stimuli, the hidden defect does not produce any change in surface temperature. Under external heating, heat conduction takes place inside the test piece. The presence of a defect perturbs the conduction path resulting abnormal surface temperature profile.

Depending on the nature of external heating, active tests are divided into various categories, e.g., pulsed thermography (PT),[1,2] lock-in thermography (LT),[3,4] frequency modulated thermal wave imaging (FMTWI),[5,6] vibro-thermography, and eddy current thermography. In PT, LT, and FMTWI, the heating is applied in the form of heat itself. In vibro-thermography and eddy current thermography, heat is generated due to friction caused vibration or due to Joule heating caused by induced alternating current, respectively.

Using thermal imaging, a sub-surface defect cannot be captured directly. Instead, its presence has to be inferred from the abnormal variation in the observed surface temperature profile of the test piece. For qualitative inspection, only visual interpretation of the thermal images is sufficient. However, quantitative inspection needs mathematical processing tools, which either rely on some analytical heat-flow model of the test piece, or numerical simulation. The analytical modelling is feasible when the test piece has a well-behaved geometry. This poses a challenge for complex shaped real objects, which can only be tackled by numerical simulation.

Numerical simulations essentially rely on finite element modelling. Electro-thermal modelling, as described in Sec. II, is not an exception in that sense. It exploits mathematical similarity between heat flow and current flow to map the problem into an electrical simulation problem. Hence known results from electrical circuits, e.g., series and parallel combination of RC network impedance, can be directly used. This is the key advantage of electro-thermal modelling. This becomes evident while optimizing the mesh size which has been discussed in Sec. III. The time evolution of the voltages present at various nodes of a given RC-network is described in Sec. IV. This section also talks about issues in simulation time stepping. Finally, the proposed concepts are verified against lock-in thermography experimental data using a piece of carbon fibre reinforced plastic (CFRP) with back drilled holes. The sample and the excitation frequencies are so chosen that it demonstrates the presence of blind frequency[7,8]—a phenomenon that cannot be explained by one dimension analytical heat flow model.

It may be mentioned that blind frequency varies with defect depth and size. At frequencies lower than that of blind frequency, a given defect manifests itself as white spot in a gray-scale phase image, while at higher frequencies it becomes black. Hence in the transition, it merges with its surroundings, making it hard to detect. The name, blind frequency, originates from this observation. Hence to overcome the drawback, lock-in thermography has to be performed at multiple frequencies.

1-D heat flow model cannot explain the blind frequency phenomenon. It is purely a 3-D heat flow effect, which can only be produced numerically using finite element modelling technique, e.g., electro-thermal model as described in this paper.

II. ELECTRO-THERMAL MODEL

Electro-thermal modelling is the study of the thermal behavior of an object by exploiting the problem's mathematical similarities to that of an electrical network of resistors and capacitors. It uses the laws of heat transfer, charge transfer, heat retention, and charge retention to predict the thermal evolution of a body. The analogy between a thermal and an electrical system are as follows:

- Temperature difference, which produces heat flow, is analogous to voltage difference which produces charge flow, i.e., current.
- Heat retention by a body is analogous to charge retention by a capacitor. The former increases the body's temperature while the latter increases the capacitor's voltage.

Figure 1(b) shows a slab of thickness ℓ and surface area A subjected to a constant temperature difference of ΔT across the surface.

It results in an one dimensional flow of heat through the material. The total heat transferred through the surface per second is

$$H_{\mathrm{cnd}} = \frac{kA}{\ell} \times \Delta T, \tag{1}$$

where k is the thermal conductivity of the material. Figure 1(a) shows an equivalent RC-network subjected to a constant voltage difference ΔV. The total charge transferred through the network per second, i.e., the current, is

$$I = I_{\mathrm{in}} = I_{\mathrm{out}} = \frac{\Delta V}{R^{\mathrm{e}}/2 + R^{\mathrm{e}}/2} = \frac{\Delta V}{R^{\mathrm{e}}}, \tag{2}$$

where $R^{\mathrm{e}}/2$ is the value of each of the resistors. The capacitor remains dormant as the applied voltage does not change with time. The mathematical similarity between Eqs. (1) and (2) leads to the equivalence

$$R^{\mathrm{e}} \equiv \frac{\ell}{kA}. \tag{3}$$

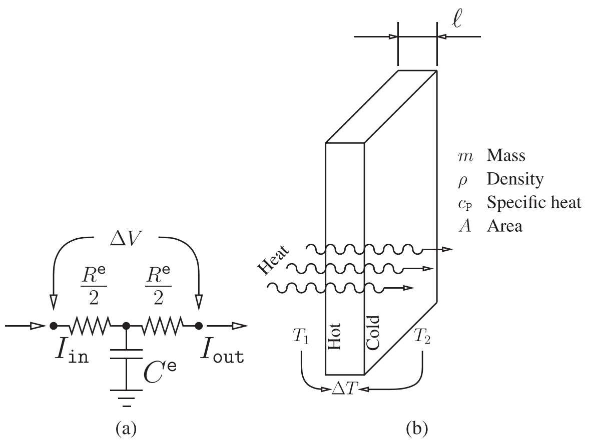

(a) (b)

FIG. 1. Analogy between electrical and thermal quantities: Electro-thermal modelling. (a) Single node RC-network. (b) One dimensional heat flow through a rectangular slab.

Further, if δH amount of heat is injected into the slab in Figure 1(b) and the heat is not allowed to come out from there, then it results in an increase in the body temperature. The temperature change and the injected heat is related by

$$\begin{aligned} \delta H &= m c_{\mathrm{P}} \delta T \\ &= (A\ell\rho c_{\mathrm{P}})\delta T, \end{aligned} \tag{4}$$

where m is the mass of the body, ρ is its density, c_{P} is the specific heat of the body material, and δT is the increase in temperature. Similarly, if δq charge is injected into the capacitor in Figure 1(a) and is forced to be retained there, the increase in the capacitor's voltage and the amount of injected charge are related by

$$\delta q = C^{\mathrm{e}} \delta V, \tag{5}$$

where C^{e} is the value of the capacitor and δV is the change in the capacitor's voltage. The mathematical similarity between Eq. (4) and Eq. (5) leads to yet another equivalence

$$C^{\mathrm{e}} \equiv A\ell\rho c_{\mathrm{P}}. \tag{6}$$

Equations (3) and (6) form the fundamental of electro-thermal modelling. Table I summarizes the theory behind the model.

III. OPTIMIZATION OF SLICE THICKNESS

In any finite element modelling, element size plays a crucial role in determining the speed and accuracy of the solution. Too big an element size causes erroneous results, while too small an element size slows down the calculation speed. It is thus necessary to optimize the element size so that the calculation runs at maximum possible speed without causing any significant error. The same is applicable to RC-modelling. Figure 2 shows the one dimensional electro-thermal model which physically represents a semi-infinite bar like material. The values of R^{e} and C^{e} are calculated using Eqs. (3) and (6) from the thermal conductivity (k), density (ρ), and specific heat (c_{P}) of the material. Since heating is applied on the surface of a body, which is analogous to a current being applied at the outer most element of the network, its temperature response, which is analogous to voltage, can be calculated by multiplying the applied current with the reactance of the network (X_{net}). This demonstrates the advantage of electro-thermal modelling, where known

TABLE I. Analogy between electrical and thermal models.

Electrical model	Thermal model	Analogy
Law of resistor		
Current (I)	Heat flow (H_{cnd})	$R^{\mathrm{e}} \equiv \ell/kA$
Voltage difference (ΔV)	Temperature difference (ΔT)	
$I = (1/R^{\mathrm{e}}) \times \Delta V$	$H_{\mathrm{cnd}} = (kA/\ell) \times \Delta T$	
Law of capacitor		
Change in voltage (δV)	Change in temperature (δT)	$C^{\mathrm{e}} \equiv A\ell\rho c_{\mathrm{P}}$
Charge transferred (δq)	Heat transferred (δH)	
$\delta q = C^{\mathrm{e}} \times \delta V$	$\delta H = (A\ell\rho c_{\mathrm{P}}) \times \delta T$	

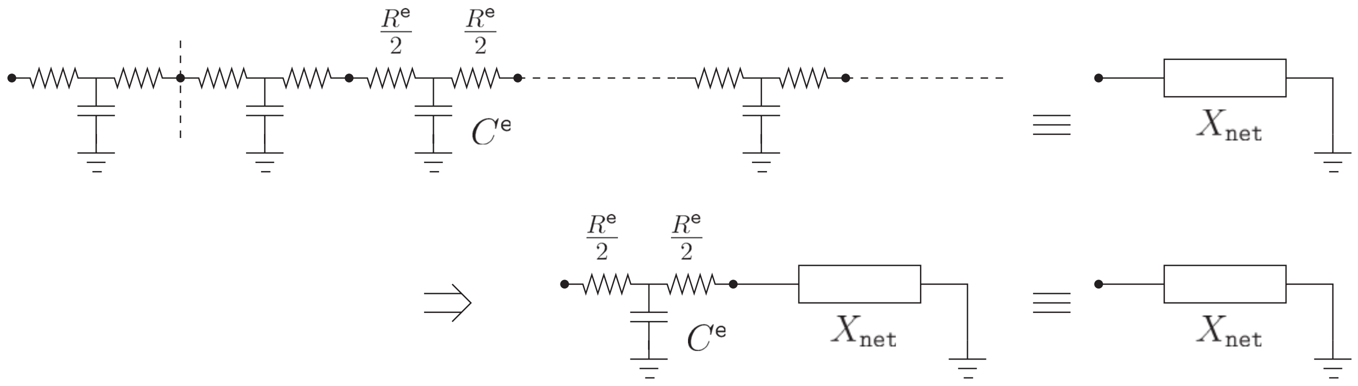

FIG. 2. 1D infinite RC network and its equivalent representation for analytical impedance calculation.

results from electrical circuit can be applied. It is not obvious in any other finite element technique.

If X_{net} is complex, the voltage response suffers a phase shift with respect to the excitation current. This phase shift is analogous to the phase lag between periodic heating excitation and resultant oscillating surface temperature of a body. To find X_{net}, the outer most node is isolated. Being an infinite series of RC, this isolation does not affect the reactance of the remaining network, and hence it can be replaced with X_{net}. This leads to the following equation:

$$\begin{aligned} X_{net} &= \frac{R^e}{2} + \left[X_C \middle\| \left(\frac{R^e}{2} + X_{net} \right) \right] \\ \Rightarrow X_{net}^2 &= \left(\frac{R^e}{2} \right)^2 + R^e X_C, \end{aligned} \tag{7}$$

where $X_C = -i/C^e\omega =$ the reactance of the capacitor, and ω is the angular excitation frequency. Putting the expression of R^e and C^e from Eqs. (3) and (6), respectively

$$X_{net}^2 = \left(\frac{\ell}{2kA_{crs}} \right)^2 + \frac{\ell}{kA_{crs}} \times \frac{-i}{A_{crs}\ell\rho c_P\omega}. \tag{8}$$

If ℓ is expressed as β fraction of the thermal diffusion length ($\mu = \sqrt{2k/\rho c_P\omega}$), then replacing ℓ with $\beta\mu$, and $\rho c_P\omega$ with $(2k/\mu)^2$ in Eq. (8) yields

$$X_{net}^2 = \left(\frac{\beta\mu}{2kA_{crs}} \right)^2 - \frac{i}{2} \left(\frac{\mu}{kA_{crs}} \right)^2. \tag{9}$$

On simplification, it becomes

$$X_{net}^2 = \frac{1}{2} \left(\frac{\mu}{kA_{crs}} \right)^2 \sqrt{1 + \frac{\beta^4}{4}} \times e^{i\phi}, \tag{10}$$

where $\phi = \tan^{-1}(-2/\beta^2)$. Thus the expression of X_{net} becomes

$$X_{net} = Qe^{i\theta},$$

where its amplitude (Q) is given by

$$Q = \frac{1}{\sqrt{2}} \left(\frac{\mu}{kA_{crs}} \right) \left(1 + \frac{\beta^4}{4} \right)^{\frac{1}{4}}, \tag{11}$$

and its phase (θ) is given by

$$\theta = \frac{1}{2} \tan^{-1}(-2/\beta^2). \tag{12}$$

If the material is progressively sliced into finer elements, i.e., $\beta \to 0$, then $Q \longrightarrow \mu/kA_{crs}\sqrt{2}$ and $\theta \longrightarrow -45^o$.

For a bar with unit cross-section area, the magnitude of the complex impedance can be written as

$$\begin{aligned} Q &= \frac{\mu}{k\sqrt{2}} \\ &= \sqrt{\frac{2k}{\rho c_P\omega}} \times \frac{1}{k\sqrt{2}} \\ &= \frac{1}{e\sqrt{\omega}}, \end{aligned} \tag{13}$$

where $e = \sqrt{k\rho c_P}$ is the effusivity of the material.

This satisfies the analytical solution of 1-D heat equation[9,10] which states the amplitude of surface temperature oscillation (T_{AC}) is mathematically related to the AC peak power per unit surface area (W_0) by

$$T_{AC} = \frac{W_0}{e\sqrt{\omega}}. \tag{14}$$

A plot of Eq. (12) is shown in Figure 3(a). It shows that the phase tends to -45° as the body is progressively sliced into finer elements. However, for all practical purposes, 10% of μ can be taken to be the upper limit of slice thickness. For more accurate result, $\ell = 1\%$ of μ might be the right choice. However, it considerably increases the simulation time.

The aforesaid finding is valid only for an infinite 1-D object. However, real objects are finite. Hence a plot of surface phase (θ) as a function of object thickness (L) needs to be given. This has been done by truncating the infinite R-C chain, and finding the argument (θ) of its resultant complex impedance. Figure 3(b) shows a plot of θ as a function of L, which has been generated by fixing the slice thickness to 10% of μ. It may be noted that for very thin objects, the surface temperature exhibits -90° phase shift, while for thermally thick object it is -45°. For practical purpose, a body with thickness twice the thermal diffusion length may be considered as a semi-infinite medium.

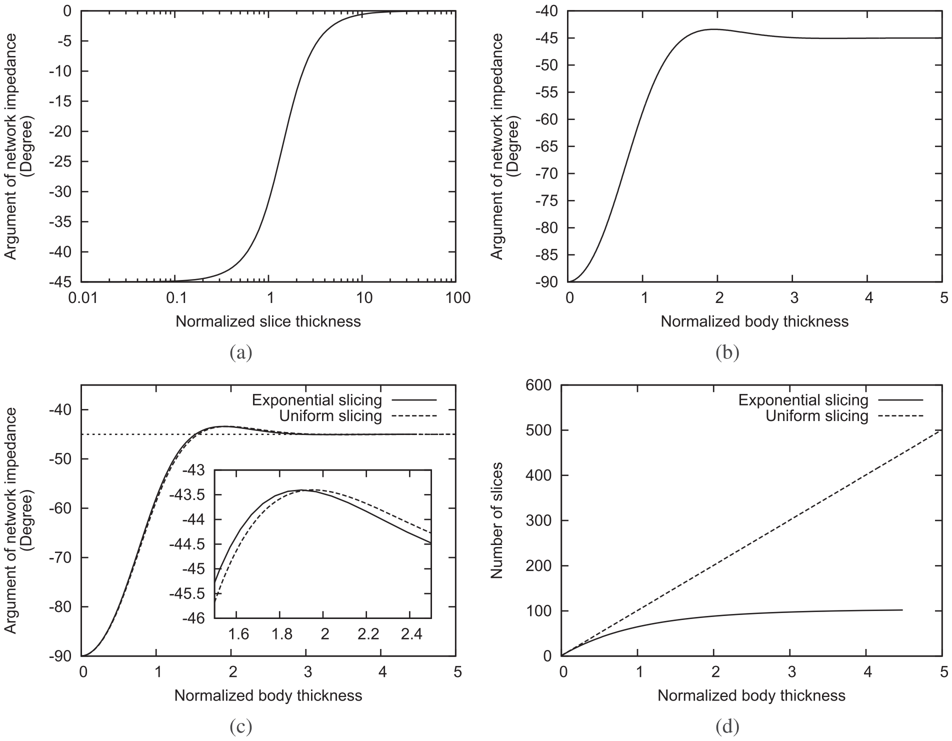

(a) (b) (c) (d)

FIG. 3. Optimization of slice parameters in finite element modelling. (a) Phase shift vs. (ℓ/μ). (b) Phase shift vs. (L/μ) when the body is divided into slices of equal thickness $\ell = 10\%$ of μ. (c) Phase shift vs. (L/μ) when the body is divided into slices with exponentially increasing thickness. The dotted line, obtained from uniform slicing, is given for comparison. (d) Total number of slices vs. (L/μ) for uniform and exponential slicing scheme.

So far the body is sliced into equal thickness. However, the model yields almost identical result had the body been sliced with exponentially increasing thickness along the direction of heat flow. In this scheme, the slice thickness (ℓ) of an element at a distance x from the surface will be

$$\ell = \ell_0 \exp(x/\mu), \tag{15}$$

where $\ell_0 = 10\%$ of μ. Figures 3(c) and 3(d) show the linear and exponential schemes together. For a body with thickness twice the thermal diffusion length, the exponential scheme reduces the number of nodes by a factor of two.

IV. ELECTRO-THERMAL MODELLING IN 3D

To simulate the complex heat flow inside a three dimensional real body, it is sliced into finite elements using rectangular, cylindrical, spherical, or other suitable topology. Each of these finite elements individually follows the laws of heat flow and heat retention.

Let us consider an RC-network consisting of N-nodes which are interconnected through resistors and individually hosts a grounded capacitor. No other external components are connected to the network, i.e., the network is closed in nature. Let R^{e}_{ij} is the resistance between the i-th and j-th nodes and C^{e}_k is the capacitance at k-th node. At time $t = 0$, the capacitor voltages are $\{V_k\}$, where $k = 1, 2, \ldots, N$. Consequently the current through the resistor between the i-th and j-th nodes is

$$I_{ij} = \frac{(V_i - V_j)}{R^{\mathrm{e}}_{ij}}. \tag{16}$$

Thus, at $t = 0$, the total current entering the k-th node is

$$I_k = \sum_{\substack{i=1\\ i\neq k}}^{N} I_{ik} = \sum_{\substack{i=1\\ i\neq k}}^{N} \frac{V_i - V_k}{R^{\mathrm{e}}_{ik}}. \tag{17}$$

In order to satisfy, the law of conservation of charge, a balancing current must flow out from each of the nodes to their associated capacitor. Thus, in next Δt time, the total charge transferred to the k-th capacitor is

$$\delta q_k = I_k \times \Delta t. \tag{18}$$

These charges change the voltages of the capacitors by $\delta V_k = \delta q_k / C^{\mathrm{e}}_k$. Thus the capacitor voltages at $t = \Delta t$ will be

$$V_k|_{t=\Delta t} = V_k|_{t=0} + \delta V_k. \tag{19}$$

These capacitor voltages become the starting point of a similar calculation cycle to predict the system's behavior at $t = 2\Delta t$ and so on. Of course, the prediction, which is linear in nature, is meaningful only when $\Delta t \rightarrow 0$. In practice, the optimum time step is found to be $(R^{\mathrm{e}})^{\mathrm{eq}}_k \times C^{\mathrm{e}}_k$ where $(R^{\mathrm{e}})^{\mathrm{eq}}_k$ is the equivalent resistance seen from the k-th node. In case, $(R^{\mathrm{e}})^{\mathrm{eq}}_k \times C^{\mathrm{e}}_k$ vary from node to node, their minimum is taken as the optimum time step. Taking longer step would result in diverging solution.

The network described above does not draw any current from external devices. However in active thermography, the object is intentionally heated by means of external heat sources. In the context of electro-thermal modelling, such heat sources are represented by current sources that feed the network nodes. This makes the network open in nature. To analyze such a system, the external currents are added to the right hand side of Eq. (17) while calculating the net incoming currents at a node. Thus

$$I_k = \left(\sum_{\substack{i=1\\ i\neq k}}^{N} I_{ik} \right) + I_{\mathrm{ext},k} = \left(\sum_{\substack{i=1\\ i\neq k}}^{N} \frac{V_i - V_k}{R^{\mathrm{e}}_{ik}} \right) + I_{\mathrm{ext},k}. \tag{20}$$

The rest of the analysis remains as it was in the case of closed network. Schematically the iteration steps are

$$V_i\Big|_t \xrightarrow[I_{\text{ext},k}]{R^{\text{e}}_{ik}} I_k\Big|_t \xrightarrow{\Delta t} \delta q_k\Big|_t \xrightarrow{C^{\text{e}}_k} \delta V_k\Big|_t \longrightarrow V_k\Big|_{t+\Delta t}. \tag{21}$$

V. VALIDATION OF THE SIMULATOR ON A CFRP TEST PIECE

The simulator was deployed to simulate circular defects in CFRP and the results are verified experimentally. Figure 4(a) shows a drawing of the sample which was used for experimental verification of the simulator. The corresponding experimental setup is shows in Figure 4(b). The test piece was periodically heated with two 1 kW tungsten-halogen flood lamps. IR screens, consisting of glass tanks containing water (30 mm of water and 5 mm glass on each side), were used to remove the IR radiation emitted by the flood lamps that may have interfered with the lock-in tests. Also, a smaller 500 W reference lamp was placed inside the setup which is seen through two glass reflectors to cut down its intensity. All phase values reported in this experimental work are measured with respect to this reference lamp. The thermal images were recorded with a Indigo Merlin camera and ThermoScope system.

The test piece has four flat bottomed hole series having 2 mm, 4 mm, 6 mm, and 12 mm diameter. Each of the first three hole series spans depths from 0.25 mm to 2.75 mm in steps of 0.25 mm, while the four 12 mm diameter holes at the edge of the sample are at depths of 2, 2.5, 3, and 3.5 mm. For this experimental work five shallowest 6 mm diameter holes were considered. They have been marked by a rectangle in Figure 4(a). They were chosen because the blind frequency effect was most prominent in their lock-in phase images. It may be mentioned that the same experiment data was originally published by the authors in an independent work where three thermal imaging techniques, *viz.,* pulsed, lock-in, and frequency modulated thermography, were objectively compared.[10]

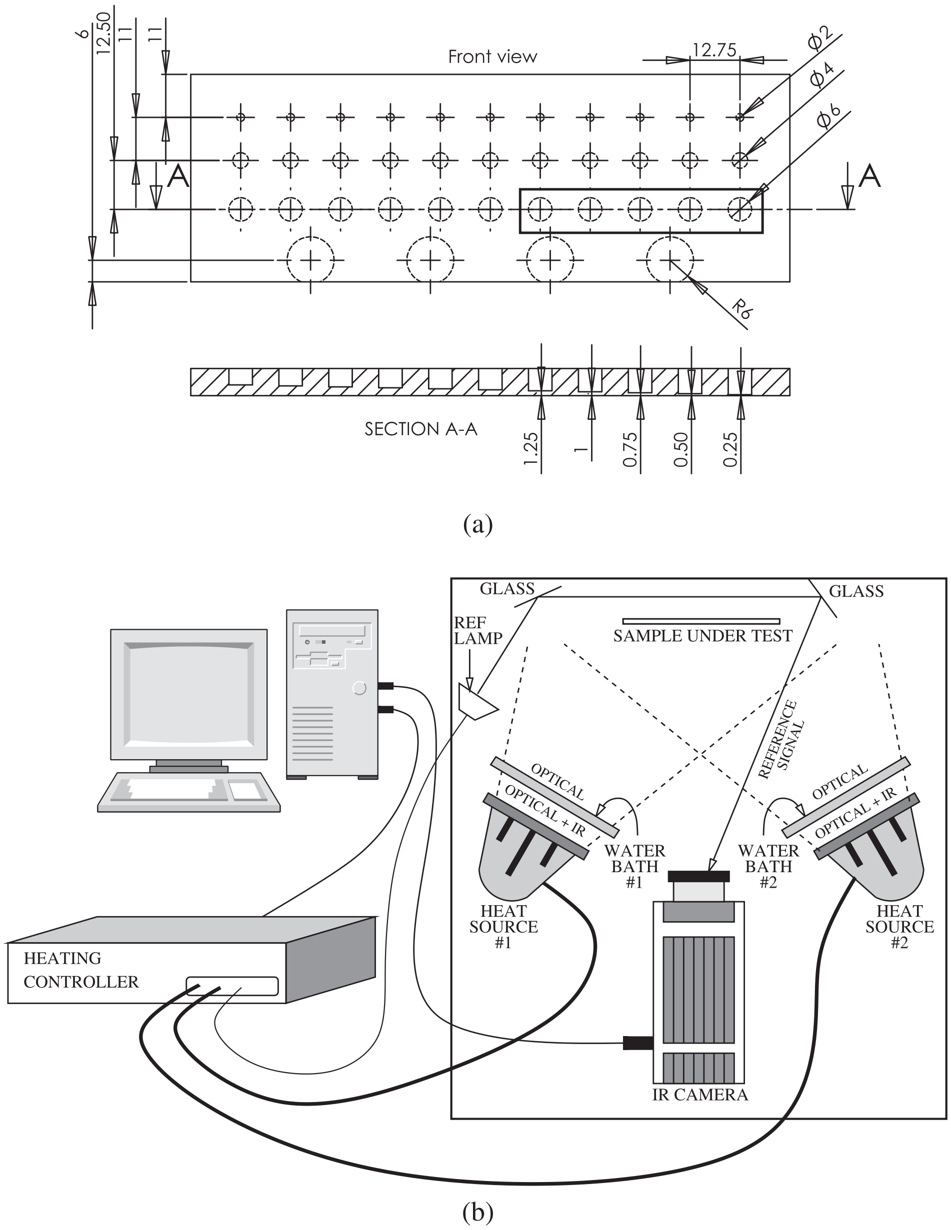

(a)

(b)

FIG. 4. Test piece and experimental setup. (a) A drawing of the CFRP test piece used for comparison studies (all dimensions are in mm). (b) The experimental setup for lock-in thermography experiment.

Since CFRP exhibits anisotropy, the bulk thermal conductivities parallel ($k_\parallel$) and perpendicular ($k_\perp$) to the fibre needed to be entered in the simulation. The typical value of the thermal conductivity of a single carbon fibre along its length was reported[11] to be in the order of $7\,\mathrm{W\ m^{-1}\ K^{-1}}$, while in the perpendicular direction it is $2\,\mathrm{W\ m^{-1}\ K^{-1}}$. In addition, the thermal conductivity of the homogeneous resin was reported to be $0.23\,\mathrm{W\ m^{-1}\ K^{-1}}$. For a typical CFRP material having 40% resin and 60% carbon fibre, the thermal conductivity along the fibre length was calculated by the rule of mixture. It states the effective thermal conductivity (k_{eff}) of a mixture of resin and carbon fibre in the volumetric proportion of $\beta_{\mathrm{res}} : \beta_{\mathrm{fib}}$ would be

$$k_{\mathrm{eff}} = \beta_{\mathrm{res}} k_{\mathrm{res}} + \beta_{\mathrm{fib}} k_{\mathrm{fib}}, \tag{22}$$

where k_{res} and k_{fib} are the thermal conductivities of resin and carbon fibre, respectively. With this formula the thermal conductivity of CFRP, parallel to the fibre length ($k_\parallel$) was

$$k_\parallel = 0.6 \times 7 + 0.4 \times 0.23 \approx 4.3\,\mathrm{W\,m^{-1}\,K^{-1}}. \tag{23}$$

The thermal conductivity of CFRP, perpendicular to the fibre length ($k_\perp$) for a 40% : 60% :: resin : fibre mixture was reported[11] to be $0.8\,\mathrm{W\ m^{-1}\ K^{-1}}$. Further the diffusivity and effusivity of commercially available black paint were reported[12] to be $2 \times 10^{-7}\ \mathrm{m^2\ s^{-1}}$ and $3000\,\mathrm{J\ K^{-1}\ m^2\ s^{-1/2}}$, respectively. These values are tabulated in Table II. To simulate a 6 mm wide cylindrical defect, at depths ranging from 0.25 mm to 1.25 mm from the surface, a 10 mm tall, 30 mm wide cylindrical CFRP body was considered. The cylindrical body was placed in such a way that the Z-axis coincided with the cylinder's axis, and its bottom surface rested on the XY-plane. A 6 mm wide flat bottomed back drilled hole was then created at the centre to depict the defect. The depth of the hole was varied, such that the defect depth ranged from 0.25 mm to 1.25 mm in steps of 0.25 mm. In addition, the top surface of the body was also painted with a 30 μm thick layer of black paint.

TABLE II. Parameters used in CFRP simulation.

Body parameters	
Diameter	30 mm
Thickness	10 mm
Material	CFRP
K (lateral)	$4.3\,\mathrm{W\ m^{-1}\ K^{-1}}$
K (transverse)	$0.8\,\mathrm{W\ m^{-1}\ K^{-1}}$
Density	$1600\,\mathrm{kg\ m^{-3}}$
Specific heat	$1200\,\mathrm{J\ kg^{-1}\ K^{-1}}$
Defect parameters	
Diameter	6 mm
Depth	0.25 mm to 1.25 mm in steps of 0.25 mm
Paint parameters	
Thickness	30 μm
Diffusivity	$2 \times 10^{-7}\ \mathrm{m^2\ s^{-1}}$
Effusivity	$3000\,\mathrm{J\ K^{-1}\ m^2\ s^{-1/2}}$
Simulation parameters	
Excitation Frequency	16.66 mHz to 83.33 mHz in steps of 16.66 mHz
Sampling frequency	10 Hz
Duration	60 s

To speed up the simulation, the problem was reduced to a 2-dimensional simulation problem by exploiting the cylindrical symmetry as shown in Figure 5. In this cylindrically symmetric geometry, an annular portion of the body around the Z-axis having rectangular cross-section area can be mapped to a planner rectangle in a 2-dimensional plane. Let's call this plane YZ-plane due to its similarity of the YZ-plane of the 3-dimensional space. If the centre of the annular ring is r distance away from the axis, and its cross-section spans Δr distance in the radial direction, and Δz distance in the Z-direction, then the inner and outer radius (r_{in} and r_{out}) would be

$$r_{\mathrm{in}} = r - \Delta r/2$$
$$r_{\mathrm{out}} = r + \Delta r/2.$$

Hence the inner and outer surface area (A_{in} and A_{out}) would be

$$A_{\mathrm{in}} = 2\pi r_{\mathrm{in}} \times \Delta z$$
$$A_{\mathrm{out}} = 2\pi r_{\mathrm{out}} \times \Delta z.$$

The top and the bottom surface area (A_{z}) would be

$$A_{\mathrm{z}} = \pi(r_{\mathrm{out}}^2 - r_{\mathrm{in}}^2).$$

And the volume (ΔV) of the annular region would be

$$\Delta V = \Delta r \times \Delta z \times 2\pi r.$$

Consequently, for the aforesaid annular region, the radially inwards and outwards resistances ($R^{\mathrm{e}}_{\mathrm{in}}$ and $R^{\mathrm{e}}_{\mathrm{out}}$) would be

$$R^{\mathrm{e}}_{\mathrm{in}} = (\Delta r/2)/(k_\parallel A_{\mathrm{in}})$$
$$R^{\mathrm{e}}_{\mathrm{out}} = (\Delta r/2)/(k_\parallel A_{\mathrm{out}}).$$

The vertical resistance ($R^{\mathrm{e}}_{\mathrm{z}}$) would be

$$R^{\mathrm{e}}_{\mathrm{z}} = (\Delta z/2)/(k_\perp A_{\mathrm{z}}).$$

And the capacitance (C^{e}) would be

$$C^{\mathrm{e}} = \rho c_{\mathrm{P}} \Delta V.$$

It is worth mentioning that the dangling resistors at the boundary are placed inwards. Thus the values of these resistors are $R^{\mathrm{e}}_{\mathrm{in}} + R^{\mathrm{e}}_{\mathrm{out}}$ in the radial direction, and $2R^{\mathrm{e}}_{\mathrm{z}}$ in Z-direction (refer to ❶ in Figure 5). 60 s simulations of lock-in thermography at five frequencies which were integral multiples of 1/60 Hz, i.e., 16.66 mHz, 33.33 mHz, 50 mHz, 66.67 mHz, and 83.33 mHz, were performed. Once again, these frequencies were chosen to synchronize the simulation with the experimental verification. The required mesh sizes, which is 10% of the thermal diffusion lengths at the excitation frequencies, are tabulated in Table III. It is note worthy that the paint layer had a finer mesh than the CFRP layer.

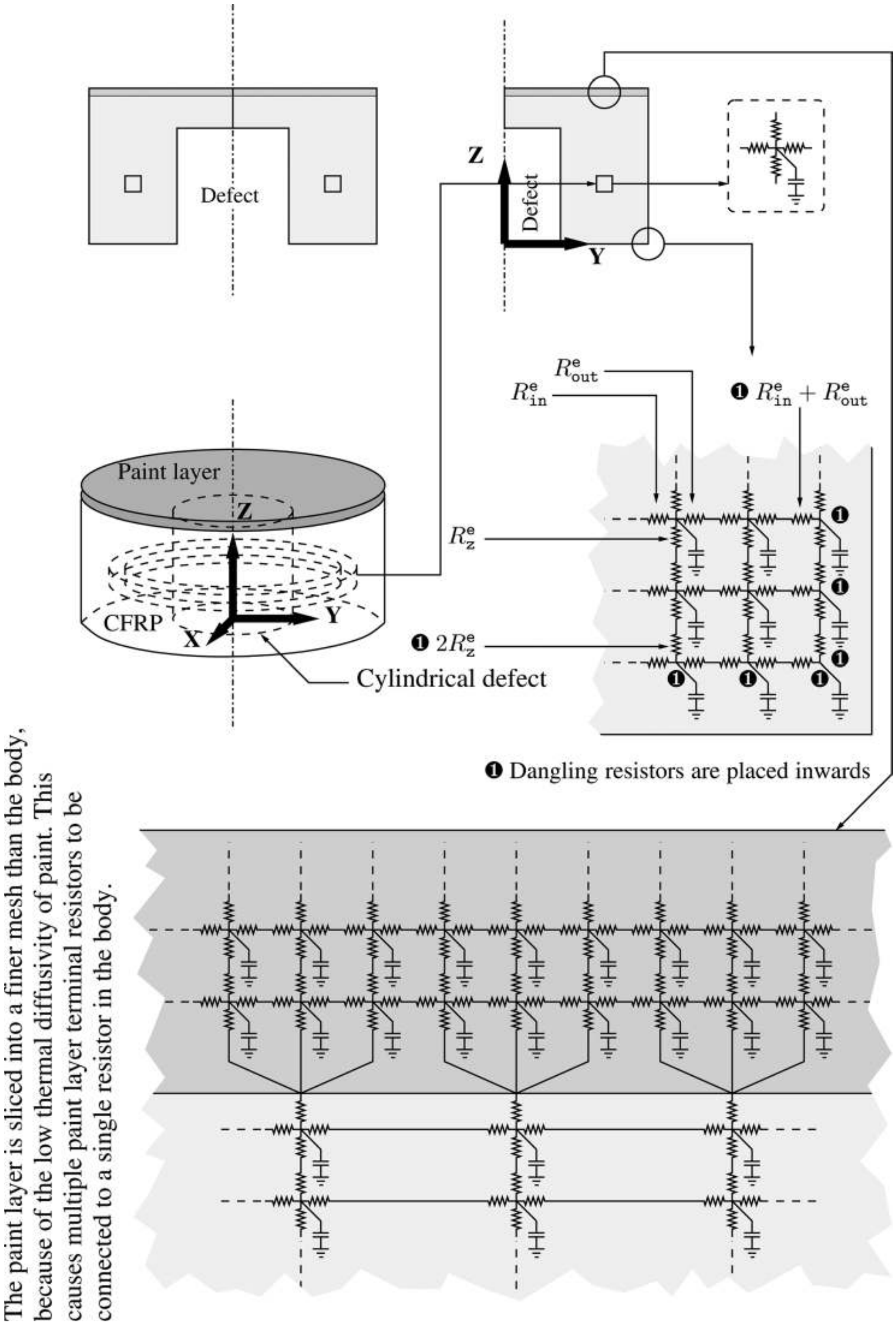

FIG. 5. Modelling of a cylindrical defect in CFRP sample using cylindrical coordinate system.

This caused multiple paint layer nodes to be connected to a single CFRP layer node as shown in Figure 5.

The simulation was performed with the parameters shown in Table II. The simulated phase images of 6 mm diameter defects in CFRP are shown in Figure 6(a). The simulation result clearly shows the blind frequency effect[7,8] for the 0.25 mm deep defect, as its colour changed from white to black with the increasing excitation frequency. This is in agreement with the experimentally observed phase images of similar defects (Figures 6(d)–6(h)). Further, Figure 6(b) shows the simulated phase vs. frequency plots as a function of excitation frequency. This is also in agreement to experimentally observed plots (Figure 6(c)).

TABLE III. Optimized mesh sizes used in CFRP simulation.

Frequencies	16.66 mHz	33.33 mHz	50 mHz	66.67 mHz	83.33 mHz
CFRP (‖)	646 μm	457 μm	373 μm	323 μm	289 μm
CFRP (⊥)	282 μm	199 μm	163 μm	141 μm	126 μm
Paint	195 μm	138 μm	113 μm	97 μm	87 μm

VI. CONCLUSION

A thermal simulator based on electro-thermal model has been designed, implemented, and demonstrated. The optimum element size of the test piece is found to be 10% of

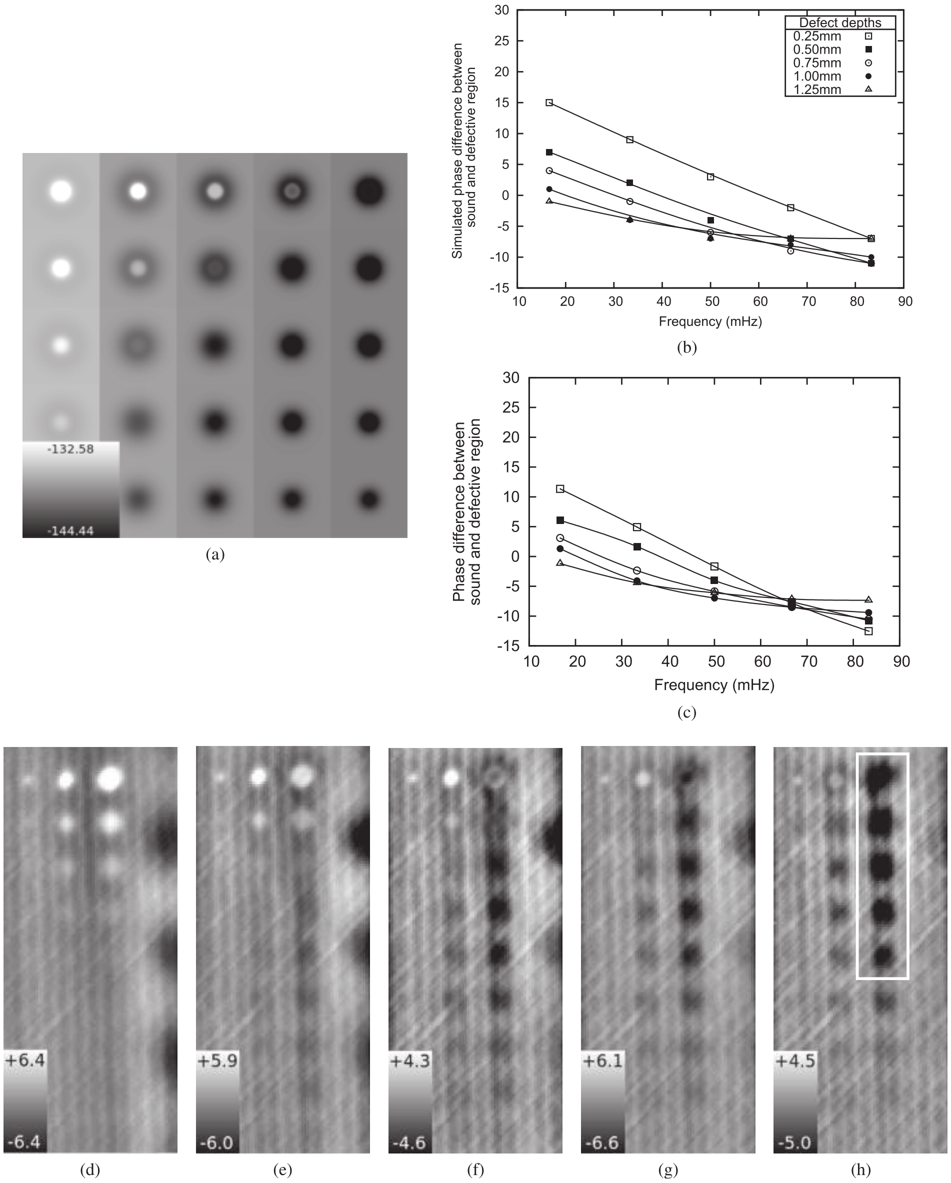

FIG. 6. Comparison of simulated and experimental phase images of defects in CFRP test piece. (a) Simulated phase images of CFRP sample at 16.7 mHz (extreme left), 33.3 mHz, 50.0 mHz, 66.7 mHz, and 83.3 mHz (extreme right). (b) Simulated phase vs. frequency plot of CFRP sample as a function of defect depths. (c) Experimentally obtained phase vs. frequency plot of CFRP sample as a function of defect depth. (d)–(h) Experimentally observed phase images at 16.6 mHz, 33.3 mHz, 50 mHz, 66.7 mHz, and 83.3 mHz, respectively.

thermal diffusion length. This produces -45° phase shift of the surface temperature oscillation with respect to excitation heat flux. In this regard, a body thicker than two times the thermal diffusion length can be treated as thermally thick. Exponential slicing scheme may be adapted for thicker bodies without any loss of simulation data quality. The optimum simulation time step is found to be in the order of thermal capacitance times effective thermal resistance seen from a given cell. The simulator is deployed to simulate circular defects in CFRP. The defects' diameter was chosen to be 6 mm which produces blind frequency effect in the frequency range of 20 mHz to 80 mHz. This phenomenon is predicted by the simulator showing its validity and usefulness.

[1] J. M. Milne and W. N. Reynolds, "The non-destructive evaluation of composites and other materials by thermal pulse video thermography," Proc. SPIE **0520**, 119–122 (1985).

[2] S. K. Lau, D. P. Almond, and J. M. Milne, "A quantitative analysis of pulsed video thermography," NDT & E Int. **24**, 195–202 (1991).

[3] G. Busse, D. Wu, and W. Karpen, "Thermal wave imaging with phase sensitive modulated thermography," J. Appl. Phys. **71**, 3962 (1992).

[4] D. Wu and G. Busse, "Lock–in thermography for nondestructive evaluation of materials," Rev. Gén. Therm. **37**, 693–703 (1998).

[5] S. Tuli and R. Mulaveesala, "Defect detection by pulse compression in frequency modulated thermal wave imaging," Quant. Infrared Thermography (QIRT) **2**(1), 41 (2005).

[6] S. Tuli and R. Mulaveesala, "Theory of frequency modulated thermal wave imaging for nondestructive subsurface defect detection," Appl. Phys. Lett. **89**, 191913 (2006).

[7] W. Bai and B. S. Wong, "Evaluation of defects in composite plates under convective environments using lock-in thermography," Meas. Sci. Technol. **12**, 142–150 (2001).

[8] C. Wallbrink, S. A. Wade, and R. Jones, "The effect of size on the quantitative estimation of defect depth in steel structures using lock-in thermography," J. Appl. Phys. **101**, 104907–104908 (2007).

[9] S. G. Pickering and D. P. Almond, "Matched excitation energy comparison of the pulse and lock-in thermography NDE techniques," NDT & E Int. **41**, 501–509 (2008).

[10] K. Chatterjee, S. Tuli, S. G. Pickering, and D. P. Almond, "A comparison of the pulsed, lock-in and frequency modulated thermography nondestructive evaluation techniques," NDT & E Int. **44**, 655–667 (2011).

[11] R. Rolfes and U. Hammerschmidt, "Transverse thermal conductivity of CFRP laminates: A numerical and experimental validation of approximation formulae," Compos. Sci. Technol. **54**, 45–54 (1995).

[12] O. Raghu and J. Philip, "Thermal properties of paint coatings on different backings using a scanning photo acoustic technique," Meas. Sci. Technol. **17**, 2945–2949 (2006).